



# Fabrication of tunable 1D rod-like and 3D yolk-like TiO<sub>2</sub> hierarchical architectures for efficient photocatalysis

Biyun Luo<sup>1</sup> , Weiwei Chen<sup>1</sup> , Juan Ma<sup>1</sup> , Wei Tian<sup>1</sup> , Chao He<sup>1</sup> , Anze Shui<sup>1,\*</sup> , and Bin Du<sup>1,\*</sup>

<sup>1</sup> School of Materials Science and Engineering, South China University of Technology, Guangzhou 510641, People's Republic of China

**Received:** 18 August 2019

**Accepted:** 22 November 2019

**Published online:**  
12 December 2019

© Springer Science+Business Media, LLC, part of Springer Nature 2019

## ABSTRACT

TiO<sub>2</sub> has attracted significant interest owing to their excellent photocatalytic properties. However, controlled preparation of TiO<sub>2</sub> with satisfactory morphology is still an urgent challenge in this field. In this work, tunable one-dimensional (1D) rod-like and three-dimensional (3D) yolk-like N-doped TiO<sub>2</sub> hierarchical architectures were successfully fabricated by one-step solvothermal route. A comparative study on morphological, structural and optical behavior of 1D and 3D TiO<sub>2</sub> is conducted by SEM, TEM, BET, XPS, UV–Vis DRS, photoelectrochemical and photodegradation experiments. The resultant N-doped TiO<sub>2</sub> with specific surface area of 190.8 m<sup>2</sup> g<sup>-1</sup> and 166.6 m<sup>2</sup> g<sup>-1</sup> for rod-like structure and yolk-like structure, respectively, exhibited excellent photocatalytic performance using rhodamine B (RhB), methylene blue (MB) and phenol as the degraded pollutants under visible-light irradiation. Benefiting from the direct electrical path, multiple internal reflections of light and high specific surface area, the rod-like N-doped TiO<sub>2</sub> possessed higher photocatalytic efficiency. Specifically, for rod-like N-doped TiO<sub>2</sub>, the reaction rate constant of the photodegradation for RhB, MB and phenol reached 12.1, 6.9 and 76.0 times, respectively, compared with P25. In comparison with yolk-like N-doped TiO<sub>2</sub>, the rate constant raised 1.5, 1.3 and 1.3 times. In addition, the formation mechanism of such controllable-morphology structure was also analyzed. This work suggests that the proper hierarchical structure combined with a large specific surface area plays a significant role on photocatalytic performance.

## Introduction

In recent years, TiO<sub>2</sub> has attracted tremendous interest in the field of green energy production and environmental remediation due to its abundant

reserve, stable physical and chemical properties, non-toxicity and high efficiency [1, 2]. However, considering their drawbacks of unsatisfactory solar energy absorption and rapid electron–hole recombination efficiency, the photocatalytic activity of TiO<sub>2</sub> material

Address correspondence to E-mail: shuianze@scut.edu.cn; dubin@scut.edu.cn

is very limited. Therefore, a series of strategies, including altering morphology, doping metal/non-metal elements and combining with a second semiconductor, were proposed to improve the light absorption and charge separation ability of TiO<sub>2</sub> photocatalytic materials [3–7]. Among various strategies, morphology controlling is a crucial “first step” in term of photocatalytic activities, which can lay a good foundation for subsequent modification work [8]. Moreover, the specific surface area, active sites for adsorption and conversion, charge separation performance and light harvesting are highly dependent on TiO<sub>2</sub> morphology [9–11]. Therefore, it is significant and meaningful to prepare TiO<sub>2</sub> with different morphologies for efficient photocatalysis [12–14].

Up to now, zero-dimensional (0D) TiO<sub>2</sub> particles, one-dimensional (1D) TiO<sub>2</sub> rods or wires, two-dimensional (2D) TiO<sub>2</sub> sheets and three-dimensional (3D) TiO<sub>2</sub> spheres have been successfully synthesized [15–19]. In many cases, 1D, 2D or 3D TiO<sub>2</sub> composed of primary nanobuilding blocks such as 0D nanoparticles [20–22]. Compared with traditional 0D particles, such hierarchical structures can lead to unique properties. For example, TiO<sub>2</sub> with 1D rod-like hierarchical structure can not only form finite space between internal microrods resembling Fabry–Perot resonator structure and resulting in increasing multiple internal reflections of light, but also provide direct electrical pathway for photogenerated electrons, reducing the probability of interparticle hopping and facilitating carrier transport [23–27]. In addition to 1D materials, 3D hollow-structured TiO<sub>2</sub> also has attracted significant attention for the sake of their large specific surface area, excellent multiple reflection and mass transfer capacity [28–30].

Indeed, TiO<sub>2</sub> with 1D, 2D and 3D hierarchical structures has been studied and highly praised by many different research groups. However, these research works are inclined to highlight the enhanced effect of a certain-dimensional TiO<sub>2</sub> [31]. Moreover, numerous works focused on the fabrication of TiO<sub>2</sub> with various morphologies by different methods [32–34]. Most of them cannot be compared photocatalytic performance directly due to the existence of uncertain complexity and impurity ions in synthesis system [35]. In addition, even in a particular system, most of the researches only present a certain-dimensional morphology control, such as rods, core/shell rods to hollow rods or solid spheres, core/shell

spheres to hollow spheres [36–38]. There are few reports on tuning among different-dimensional samples, making it difficult for us to directly compare and choose 1D, 2D or 3D TiO<sub>2</sub> materials. Therefore, it is highly desired to fabricate catalysts of various dimensions under the same capping agents and process to compare the photocatalytic activity.

Nitrogen doping, as a strategy to improve visible-light-driven range, has become very mature in the field of photocatalysis [39, 40]. However, most of the N-doped TiO<sub>2</sub> was prepared by multiple heat treatments for obtaining products with higher crystallinity and better N modification [41]. Such methods not only involve difficult steps and high-energy consumption, but also suffer low specific surface areas due to grain coarsening.

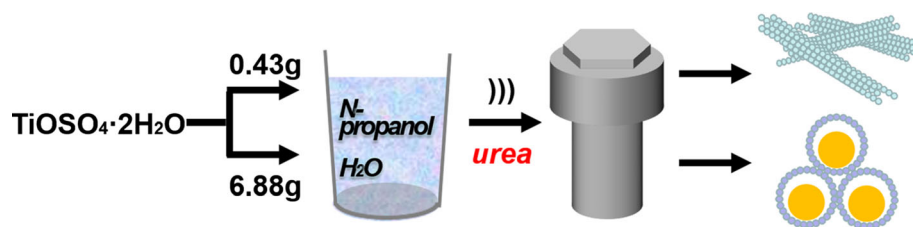
Herein, we report, for the first time, a novel green solvothermal route for controlled preparation of different-dimensional N-doped TiO<sub>2</sub> without annealing. The transforming from 1D rod-like to 3D yolk-like hierarchical architectures could be achieved by simply adjusting the amount of precursor, which can guarantee the comparability of experimental results of photocatalysis. The effect of processing conditions on the morphology is investigated, and the effect of TiO<sub>2</sub> dimensionality on the specific surface area, charge separation and photocatalytic performance is also systematically studied. This work provides a guidance for designing and controlling other hierarchical microstructures for photocatalytic degradation.

## Experimental section

### Material synthesis

The preparation process is illustrated in Fig. 1. In a typical N-doped rod-like TiO<sub>2</sub> procedure, 0.43 g of TiOSO<sub>4</sub> (Macklin) precursor was dispersed in a mixture solution of 120 mL N propanol and 40 mL deionized water and then stirred at room temperature overnight. Subsequently, the homogenous solution was sonicated for 20 min in an ultrasonic bath. Then, 0.10 g of urea was added into the solution to make sure the mole ratio of urea to TiOSO<sub>4</sub> was 0.6. Finally, the as-prepared mixture solution was transferred into a Teflon-lined stainless-steel autoclave at 90 °C for 14 h. The resultant precipitates were filtered, washed thoroughly with water and ethanol for several times and dried at 80 °C for 8 h under

**Figure 1** Synthesis procedure for the selective preparation of N-doped rod-like and yolk-like  $\text{TiO}_2$ .



electronic oven and denoted as N-TR. The N-doped yolk-like  $\text{TiO}_2$  was achieved by adding precursor and urea contents at the values of 6.88 g and 1.55 g, respectively, and denoted as N-TYS. Additionally, different precursor contents (0.86 g, 1.72 g and 3.44 g) and reaction time (0.5 h, 2 h, 14 h and 26 h) were also applied in order to investigate the evolution of the morphology. For comparison, the N-free samples were also carried out and denoted as TR and TYS, respectively.

### Characterization

The morphology of as-prepared samples was characterized by scanning electron microscopy (SEM, NOVA NanoSEM 430, the Netherlands), and the composition was examined using energy-dispersive spectroscopy (EDS, Zeiss, Oberkochen, Germany) attached to the SEM. Transmission electron microscopy (TEM) and high-resolution transmission electron microscopy (HR-TEM) were performed using FEI Tecnai G2 F20 instrument (FEI, America). The X-ray diffraction (XRD) patterns of the samples were recorded by an X-ray diffractometer (XRD, D/Max-3C, Rigaku Co., Tokyo, Japan) using  $\text{Cu K}_\alpha$  radiation ( $\lambda = 1.5418 \text{ \AA}$ ). The specific surface areas were measured from the Brunauer–Emmett–Teller (BET) plots. XPS (Thermo Scientific K-Alpha) was used to probe the binding energy distributions of the material.

### Photoelectrochemical test

Electrochemical measurements including electrochemical impedance spectroscopy (EIS) and photocurrent tests were carried out on a CHI660C electrochemical workstation (Shanghai Chenhua, China) with a conventional standard three-electrode system (Pt plate as the counter electrode,  $\text{Ag}/\text{AgCl}$  as the reference electrode, depositing samples on FTO conductive glasses as working electrode and 0.5 M  $\text{Na}_2\text{SO}_4$  aqueous solution as the electrolyte). The photocurrent tests were measured under a 500 W Xe

lamp equipped with an ultraviolet cutoff filter ( $\lambda > 420 \text{ nm}$ ) (CHF-XM, Beijing Changtuo Technology Co. Ltd, China) as the visible light. EIS plots were performed in the frequency range from  $10^{-2}$  to  $10^5 \text{ Hz}$  with amplitude of 5 mV under the 500 W Xe lamp.

### Photodegradation and active species trapping experiments

The photodegradation activity was estimated by degradation of rhodamine B (RhB), methylene blue (MB) and phenol in an aqueous solution under visible-light irradiation. A 300-W Xenon lamp with a 420 nm cutoff filter (Changtu, China) was used as irradiation source ( $\lambda > 420 \text{ nm}$ ). The distance between the lamp and the sample was 15 cm. In a typical photocatalytic degradation of RhB experiment, 50 mg of the photocatalyst was dispersed in 50 mL of RhB solution ( $10 \text{ mg L}^{-1}$ ). The suspension was stirred for 30 min in the dark to reach an adsorption–desorption equilibrium and subsequently be illuminated for different time intervals. Three milliliters of suspension was collected and centrifuged to remove the photocatalyst. The photocatalytic degradation of MB and phenol experiments was similar to that of RhB except the concentration of the dye, where a  $5 \text{ mg L}^{-1}$  MB solution and  $20 \text{ mg L}^{-1}$  phenol solution were used. The residual RhB, MB and phenol concentration was monitored via a UV–Vis spectrophotometer (UV1901PC) based on the maximum absorption at 554 nm, 664 nm and 270 nm. To investigate the reaction mechanism for photodegradation of RhB, active species trapping experiments were carried out under visible-light irradiation. The active species  $\cdot\text{O}_2^-$ ,  $\text{h}^+$  and  $\cdot\text{OH}$  were detected with the addition of benzoquinone (BQ,  $2 \text{ mmol L}^{-1}$ ), disodium ethylenediaminetetraacetate ( $\text{Na}_2\text{-EDTA}$ ,  $5 \text{ mmol L}^{-1}$ ) and isopropyl alcohol (IPA,  $10 \text{ mmol L}^{-1}$ ), respectively.

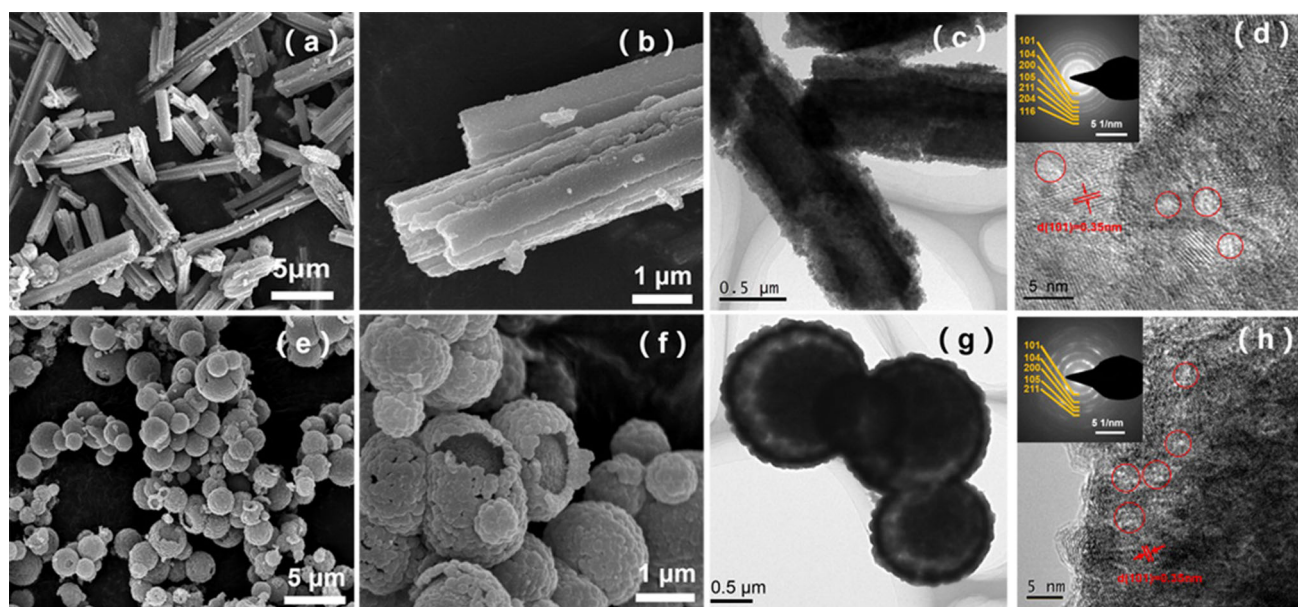
## Results and discussion

### Morphological and structural characteristics

The morphology and structure of the N-TR and N-TYS are elucidated in detail through SEM and TEM and shown in Fig. 2. As shown in Fig. 2a, rod-like shapes with tens of micrometer in length and 0.5–2  $\mu\text{m}$  in diameter are observed. Zooming into the surface of the microrod gives an impression that each rod contains several tiny rods with approximately same length (Fig. 2b). Combined with TEM image (Fig. 2c), these microrods are not completely solid. Meanwhile, considering self-assembled of these tiny rods, the interior of the microrod can form long and narrow channel, leading light into the interior easily. When increasing the precursor concentration, the well-defined yolk-like spheres with a mean diameter of 1  $\mu\text{m}$  can be observed from Fig. 2e. From the enlarged SEM image (Fig. 2f), the external surface of the shell consists of numerous single layer spherical structure, and a small core is found to be embedded in the chamber. The yolk-like structure with shell thickness  $\sim 100$  nm and the diameter of yolk 400–600 nm was clearly demonstrated in TEM image (Fig. 2g). In fact, the microrod, the shell and the core are composed of smaller particles with a diameter of  $\sim 10$  nm (as shown in Fig. S1). As the primary nanobuilding blocks, these nanoparticles self-assemble into unique 1D and 3D structures. Moreover, in

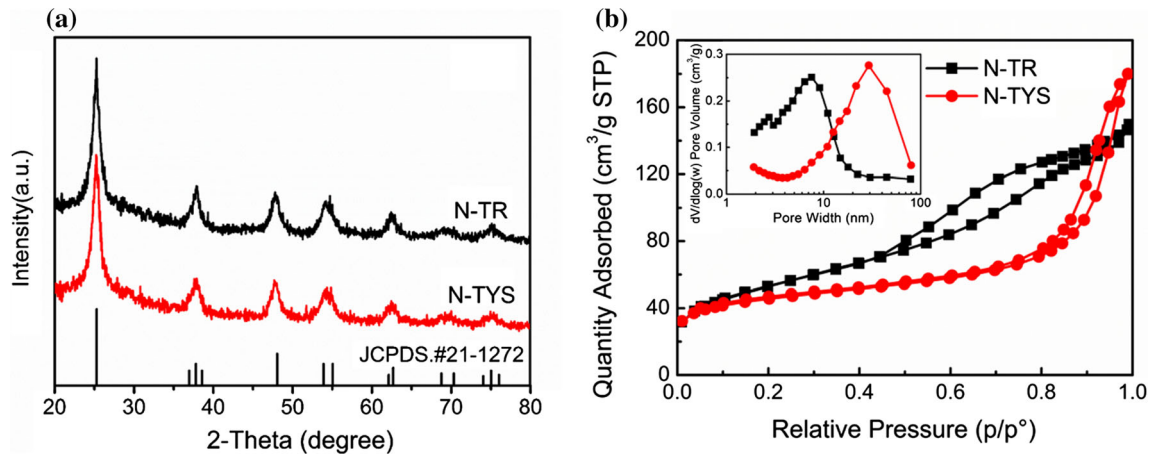
Fig. 2d and g, a great many mesopores (size of  $\sim 5$  nm) can be observed in both the structures. The lattice spacing of N-TR and N-TYS is ascertained about 0.35 nm, corresponding to the (1 0 1) plane of the anatase phase. The SAED pattern is also consistent well with the XRD pattern. However, compared with the SAED pattern of N-TR, the N-TYS is not well-defined Debye–Scherrer rings, suggesting that rod-like structure possesses higher crystallinity than yolk/shell structure. In addition, N element of N-TR and N-TYS is sufficiently confirmed by energy-dispersive X-ray spectroscopy (EDX) and depicted in detail in Supporting information (Fig. S2, Text S1). It should be pointed out that the N element barely affects the morphology of  $\text{TiO}_2$ . The SEM images of TR and TYS are displayed in Fig. S3.

Figure 3a shows the XRD patterns of N-TR and N-TYS. The peaks at  $25.24^\circ$ ,  $37.88^\circ$ ,  $47.81^\circ$ ,  $54.14^\circ$ ,  $54.92^\circ$  and  $62.53^\circ$  are observed from the two samples, presenting good agreement with the anatase phase (JCPDS card No. 21-1272). Besides, no other peaks such as N–O and Ti–N were detected in the samples, which may be ascribed to the reason that the content of N was too little to be recorded. The crystallite size is calculated based on the Scherrer formula in Table 1. The Raman spectra of N-TR and N-TYS are also examined to identify the structural properties (Fig. S4). Based on the SEM, TEM, XRD and Raman spectra, it is apparent that these  $\text{TiO}_2$  hierarchical



**Figure 2** SEM and TEM images of N-TR (a–d) and N-TYS (e–h). Insets in the HR-TEM images show the SAED pattern.





**Figure 3** **a** XRD patterns of N-TR and N-TYS; **b**  $N_2$  adsorption–desorption isotherms and (inset) the corresponding pore size distribution curves of N-TR and N-TYS.

structures present similar primary nanobuilding blocks and crystal structure but the morphology.

Figure 3b shows the nitrogen adsorption–desorption isotherms and the corresponding pore size distribution curves of the N-doped samples. The  $N_2$ -BET surface areas ( $S_{BET}$ ) for N-TR and N-TYS are calculated to be  $190.82 \text{ m}^2 \text{ g}^{-1}$  and  $166.59 \text{ m}^2 \text{ g}^{-1}$ , respectively. Although all samples show IV-type isotherm, the hysteresis loop and pore size distribution have significant differences. For rod-shaped  $TiO_2$ , the observed  $H_4$  hysteresis loop suggests the presence of slit-like pores, corresponding to the overlap among rods [42]. Furthermore, the mean pore size distribution is determined as  $\sim 4.87 \text{ nm}$ . The yolk-like structure shows  $H_1$  hysteresis loop, indicating the formation of cylindrical pores, and the average pore diameter is about  $6.7 \text{ nm}$  [42]. The summary of BET surface area, pore diameter and pore volume of the N-TR and N-TYS is depicted in Table 1. We can find that the specific surface area of N-TR is higher than that of N-TYS, but the pore size and volume of N-TR is smaller than that of N-TYS. Apparently, the difference of morphology leads to the different surface areas and porous structures.

To investigate the influence of morphology on chemical state of elements, X-ray photoemission spectroscopy (XPS) is recorded and shown in Fig. 4. The survey scan spectrum shows that N-TR and

N-TYS contain Ti, O, C and N elements, indicating that the N atom is successfully doped into the samples (Fig. 4a). After correcting with C 1s peak ( $284.8 \text{ eV}$ ), all the peaks of N-TR shift to higher binding energies, indicating the difference of morphology could slightly affect the chemical environment of elements (Fig. 4b–d). Moreover, the high-resolution N 1s peak (Fig. 4c) is carefully analyzed. By fitting the curves, four peaks can be observed. For N-TYS, the peaks at  $398.9 \text{ eV}$ ,  $399.7 \text{ eV}$ ,  $400.8 \text{ eV}$  and  $401.8 \text{ eV}$  correspond to the Pyridinic N, substitutional N for O in the form of O–Ti–N bonding and the surface adsorption of  $N_2$  and  $NO_x$  species, respectively. The result indicates that nitrogen atoms are mainly incorporated into substitutional sites of the lattice [41, 43, 44]. When changing the precursor content to obtain N-TR, the area of Pyridinic N peak significantly increases, indicating that the rod-like structure can not only introduce substitutional nitrogen but also easily form carbon and nitrogen bonding. In addition, the C 1s peak can also be analyzed (Fig. 4d). The main peak located at  $284.8 \text{ eV}$  is assigned to the C–C bonds, and the other two peaks can be fitted to C–N and O–C=O bonding [43, 45]. An apparent increase in relative intensity of C–N bonds in N-TR can be observed, which once again proved that nitrogen is easier to be introduced to bond with carbon in the microrods than yolk-like spheres. Based

**Table 1** Parameters of N-TR and N-TYS prepared with different amounts of precursor

Sample	Crystallite size (nm)	Surface area ( $\text{m}^2 \text{ g}^{-1}$ )	Pore size (nm)	Pore volume ( $\text{cm}^3 \text{ g}^{-1}$ )
N-TR	7.0	190.82	4.87	0.23
N-TYS	6.3	166.59	6.70	0.28

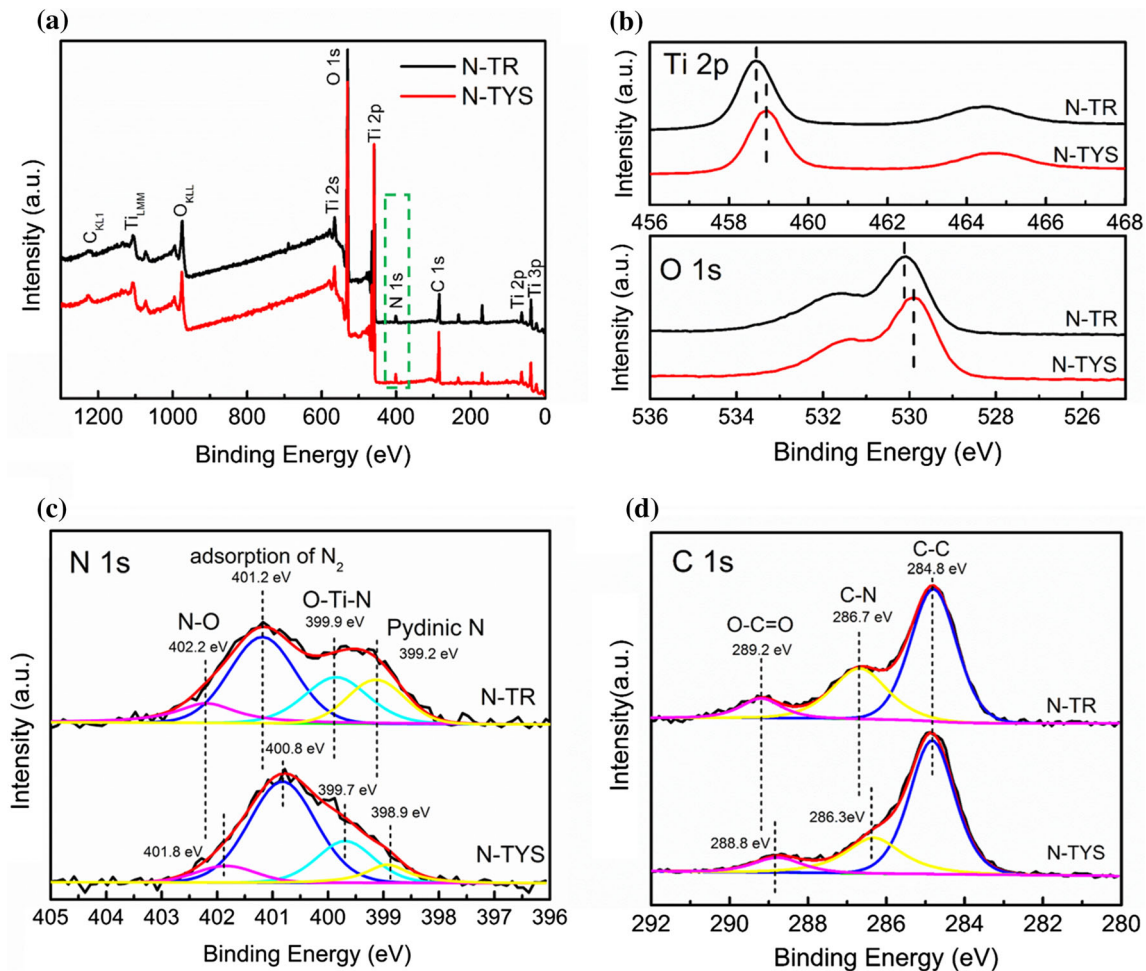


**Figure 4** **a** The integrated XPS spectrum of N-TR and N-TYS; **b** the corresponding XPS spectrums of titanium and oxygen, **c** nitrogen and **d** carbon for N-TR and N-TYS.

on the XPS analysis, the atomic ratio of nitrogen element is 3.24% in N-TR and 2.57% in N-TYS. Considering the molar ratio of  $\text{TiOSO}_4 \cdot 2\text{H}_2\text{O}$  to urea is the same and area of other N 1s peaks is similar, the above difference mainly ascribed to the bonding of carbon and nitrogen. The difference of morphology leads to different specific surface areas and mesopores structures; this may be the reason for different nitrogen incorporation conditions.

In the present case, the N-doped 1D rod-like and 3D yolk-like  $\text{TiO}_2$  hierarchical structures are successfully synthesized by only adjusting the precursor concentration. Therefore, it is necessary to explore the formation process of the two unique structures in detail. The experiments of intermediate precursor contents (0.86 g, 1.72 g, 3.44 g) are carried out and shown in Fig. 5a–c. Meanwhile, the experiments of different solvothermal reaction times (0.5 h, 2 h, 14 h,

26 h) are also illustrated and discussed in Fig. S5 and Text S2. As precursor content increases from 0.43 to 1.72 g, the morphology of the resultant  $\text{TiO}_2$  samples can be tuned from microrods to irregular aggregation of rods and spheres, which can be described in detail as a lot of messy particles appear among the microrods, and then, these microrods shorten and become thicker within the spheres growing out of the rods (Fig. 5a and b). On further increasing the concentration content to 3.44 g and 6.88 g, the rod-like structure disappears and the yolk-like structure eventually forms (Fig. 5c). Though the evolution of the morphology depends on the precursor concentration, further sufficient evidence is still needed to explain the formation mechanism of the two unique hierarchical structures. Therefore, the SEM image of  $\text{TiOSO}_4 \cdot 2\text{H}_2\text{O}$  precursor is investigated in Fig. 5d. Interestingly,  $\text{TiOSO}_4 \cdot 2\text{H}_2\text{O}$  also exhibits 1D rod-like

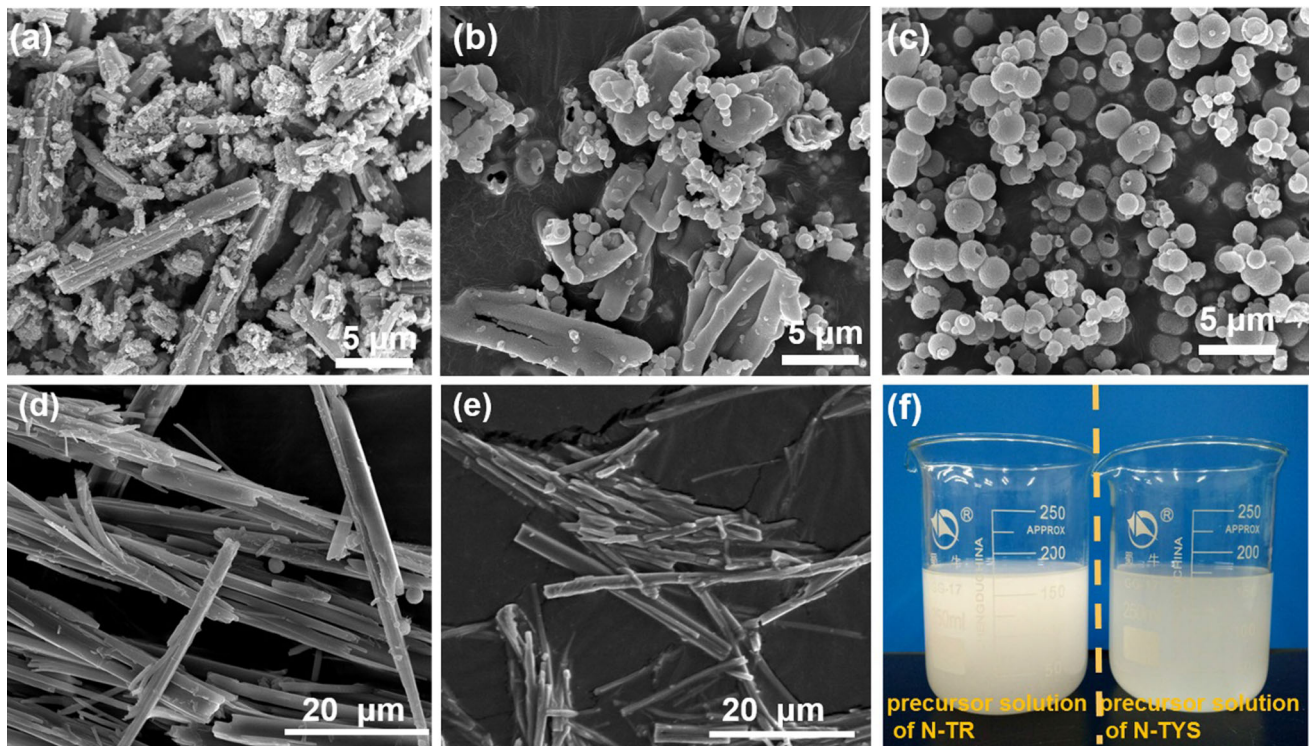


**Figure 5** SEM images of the N-doped  $\text{TiO}_2$  with different amounts of  $\text{TiOSO}_4 \cdot 2\text{H}_2\text{O}$ : **a** 0.86 g, **b** 1.72 g, **c** 3.44 g; SEM images of **d**  $\text{TiOSO}_4 \cdot 2\text{H}_2\text{O}$  and **e** the precursor solution of N-TR

which was stirred overnight; **f** photograph of titanium precursor solution of N-TR and N-TYS.

morphology. Compared with N-TR, the  $\text{TiOSO}_4 \cdot 2\text{H}_2\text{O}$  rods have smoother surface and larger aspect ratio. In addition, at low dose of precursor, the precursor solution is milky white (Fig. 5f). From the SEM image of precursor solution of N-TR (Fig. 5e), the rod-like structure is highly similar to  $\text{TiOSO}_4 \cdot 2\text{H}_2\text{O}$ . When the precursor concentration is higher than supersaturation, the solution will hydrolyze to form a white translucent suspension instead of the previous milky white suspension (Fig. 5f). Moreover, a gelatinous precipitate at the bottom of the beaker was observed. Therefore, this state should be hydrogels.

According to all above results, a possible formation mechanism of the microrods and yolk-like spheres is illustrated in Fig. 6. At the initial stage, the hydrolysis and alcoholysis reaction of  $\text{TiOSO}_4 \cdot 2\text{H}_2\text{O}$  produces nascent  $\text{TiO}_2$  nuclei. At low amounts of  $\text{TiOSO}_4 \cdot 2\text{H}_2\text{O}$ ,  $\text{TiO}_2$  nuclei follows the in situ growth mechanism [23, 46, 47]. The seeds in situ growth to form tiny rods follow the morphology of  $\text{TiOSO}_4 \cdot 2\text{H}_2\text{O}$ . As time goes on, these tiny rods assemble more closely and gradually become shorter and thicker, eventually self-assembled into rod-like hierarchical structure. At high dose of  $\text{TiOSO}_4 \cdot 2\text{H}_2\text{O}$ , the

precursor solution will undergo a sol process to form active monomers via hydrolysis and alcoholysis reaction. These active monomers gradually evolved into numerous  $\text{TiO}_2$  nanoparticles with uniform size in a chemical reaction. Due to the high surface energy, these  $\text{TiO}_2$  nanoparticles spontaneously aggregate into the spherical solid structural  $\text{TiO}_2$  [48, 49]. Thereafter, the Ostwald ripening process occurred. The nanoparticles located in the inner core have higher curvature compared with those in the outer shell. Thus, they have higher surface energies and faster dissolving rate than the shell. As a result, the nanoparticles of the inner surface will be dissolved and re-deposited on the outer surface. With the reaction time prolonged, the interior core further dissolved, and the cavity between core and shell was expanded, finally forming the well-defined yolk-like  $\text{TiO}_2$  hierarchical structure [29, 50–52]. Other transitional morphologies are formed by the combination of these two mechanisms.



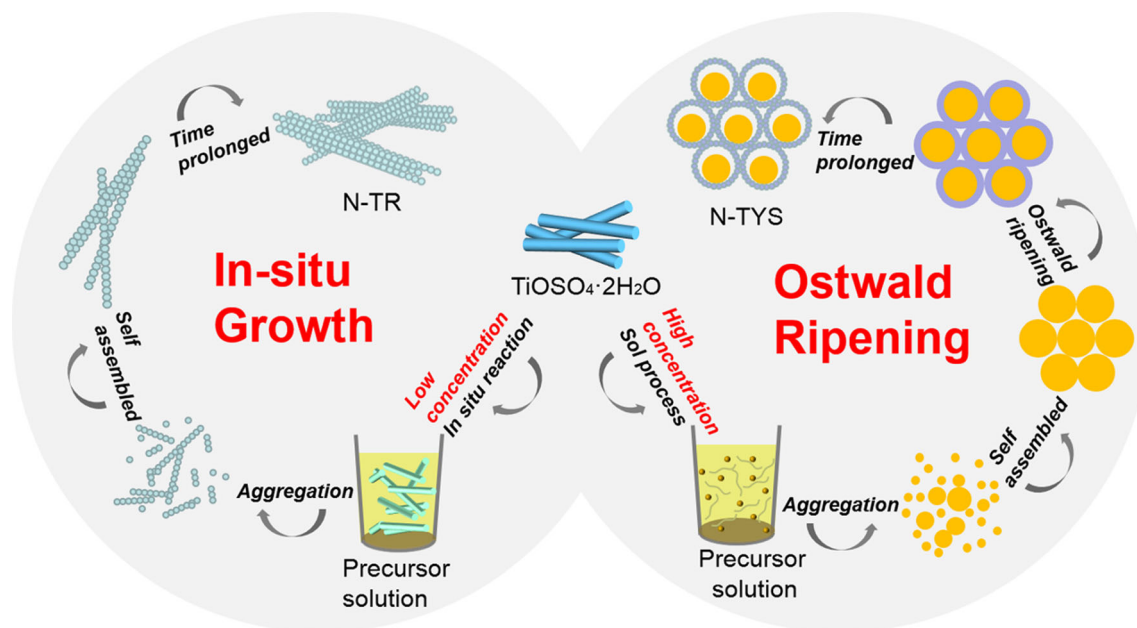


**Figure 6** Schematic illustration of the formation process for N-TR and N-TYS.

### Photocatalytic properties and mechanism

In this part, in addition to N-TR and N-TYS, a series of photocatalytic characterizations of undoped samples were also investigated under the same condition. Although the theme of this work is to discuss the influence of different-dimensional TiO<sub>2</sub> hierarchical architectures on photocatalytic performance, it is essential to know the role of nitrogen introduction in our experiment. It is generally accepted that N doping has the potential of narrowing the band gap via elevating the valence band, which further increases the visible-light response region. To investigate the influence of 1D and 3D N-doped TiO<sub>2</sub> on the optical absorption performance, UV–Vis diffuse reflectance spectra of TR, TYS, N-TR and N-TYS were recorded by UV–Vis spectrophotometer. Compared with the TR and TYS, absorption edges of N-doped samples are slightly red-shifted and their visible-light harvesting abilities increase, which can be observed clearly in Fig. 7a. For the four samples, the band gaps are estimated from plots of  $(F(R) \cdot h\nu)^{1/2}$  versus  $h\nu$ . As shown in Fig. 7b, the band gaps  $E_g$  estimated from the intercept of the tangents of the plots are determined to be 3.15 eV for both N-doped samples, while N-free samples are 3.20 eV [53]. This result confirms that the wider visible-light response region corresponds to narrower band gap. Interestingly, morphology and elemental chemical state variation have

a little influence on the band gap, which eliminate the effects of different visible-light response regions on photocatalytic activity.

The photoelectrochemical properties of the four TiO<sub>2</sub> samples were also investigated. The electrochemical impedance spectrum (EIS) was measured to investigate charge transport behaviors, and the results are shown in Fig. 8a. Whether N doping or not, the arc radius of the 1D rod-like structure is smaller than 3D yolk-like structure, suggesting that microrods have the lower resistance, higher charge mobility and separation efficiency. In addition, the transient photocurrent response curves were measured to investigate the ability of separating photo-generated electrons and holes in Fig. 8b. The photocurrent response shows a similar trend that observed from the electrochemical impedance spectrum, where the rod-like structure exhibits higher photocurrent density than yolk-like structure. In addition, the N-doped TiO<sub>2</sub> possesses higher charge separation efficiency due to the increased visible-light absorption region. In summary, different-dimensional TiO<sub>2</sub> hierarchical architectures have great impact on charge separation and transport. In this case, 1D rod-like structure is more benefit to charge separation and transport than 3D yolk-like structure, which is expected to enhance photocatalytic performance. The difference may be attributed to the fact that one-dimensional structure could provide a fast



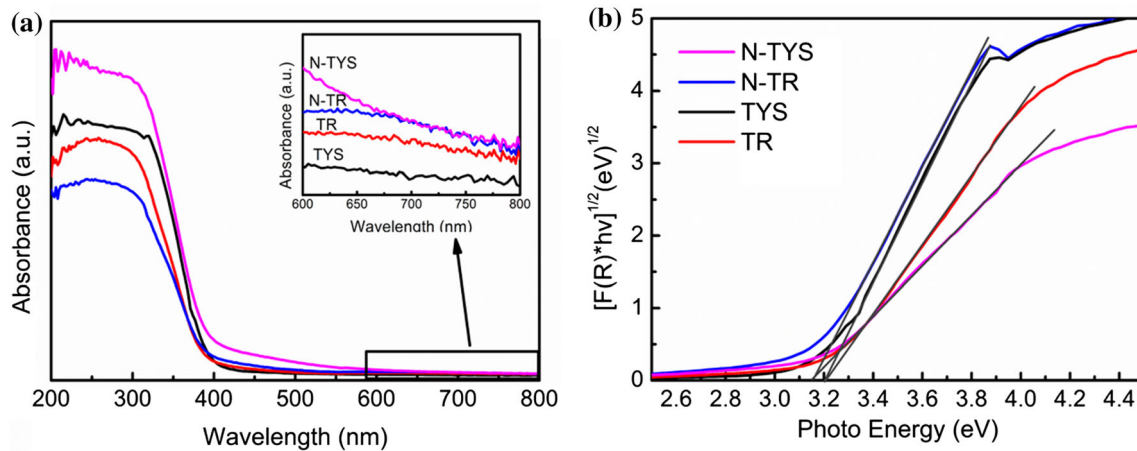


**Figure 7** **a** UV-Vis diffuse reflection spectra of TR, TYS, N-TR and N-TYS; **b** corresponding plot of transformed Kubelka-Munk function versus the light energy.

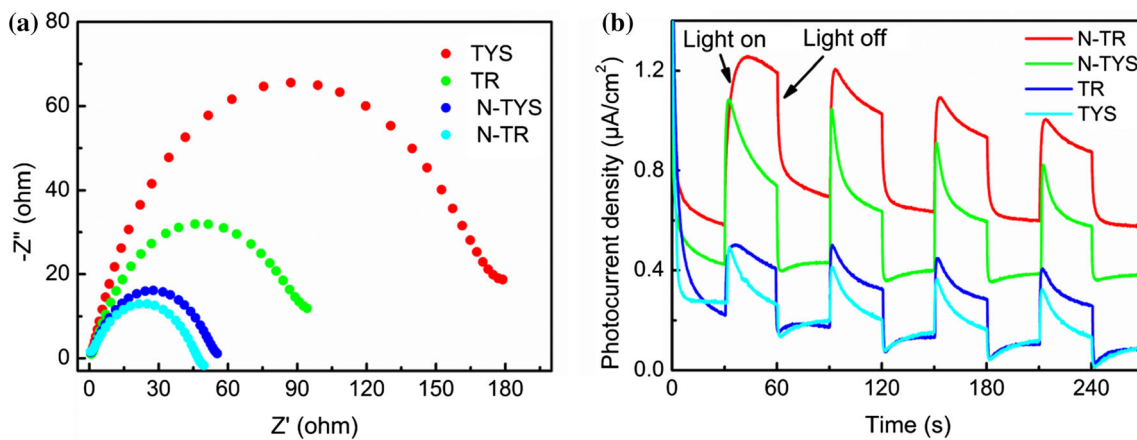


**Figure 8** **a** The EIS curves and **b** transient photocurrent response of TR, TYS, N-TR and N-TYS.

charge transport pathway, which could facilitate the electron transfer and suppress electron-hole pair recombination.

The final goal for the fabrication of unique 1D and 3D hierarchical architectures with N doping is to improve its photocatalytic property in the visible-light range. In this work, we carried out the photocatalytic degradation of RhB, MB and phenol to evaluate the photodegradation performance of TR, TYS, N-TR and N-TYS under visible-light irradiation [54]. For comparison, the degradation efficiency of P25, an excellent commercial  $\text{TiO}_2$  photocatalyst, was also investigated under the same condition. The results are shown in Fig. 9. During a 30-minute dark adsorption reaction, we found an interesting phenomenon: the adsorption of dyes for core-shell structural  $\text{TiO}_2$  is better than the rod structural  $\text{TiO}_2$ . Although the specific surface area of the core-shell

structure is slightly smaller, the pore size and pore volume are larger, which may be the reason for its better adsorption performance. But this amount of adsorption is negligible for degradation. Whether doping or not, the rod-like structure exhibits much higher RhB, MB and phenol photodegradation efficiency than yolk-like structure (Fig. 9a, c and e). In addition, P25 exhibits the lowest photodegradation activity. In order to compare the difference conveniently, the degradation kinetic model was also studied. Figure 9b, d and f shows that the relationship between time and  $\ln(C_0/C)$  is almost a straight line, which proves that the process of degradation fits the pseudo-first-order reaction [55]. The photodegradation of RhB rate constant ( $k$ ) values of P25, TYS, TR, N-TYS and N-TR is determined to be 0.0339, 0.0922, 0.1138, 0.2816 and 0.4088  $\text{min}^{-1}$ , respectively. The photodegradation of MB rate constant values is

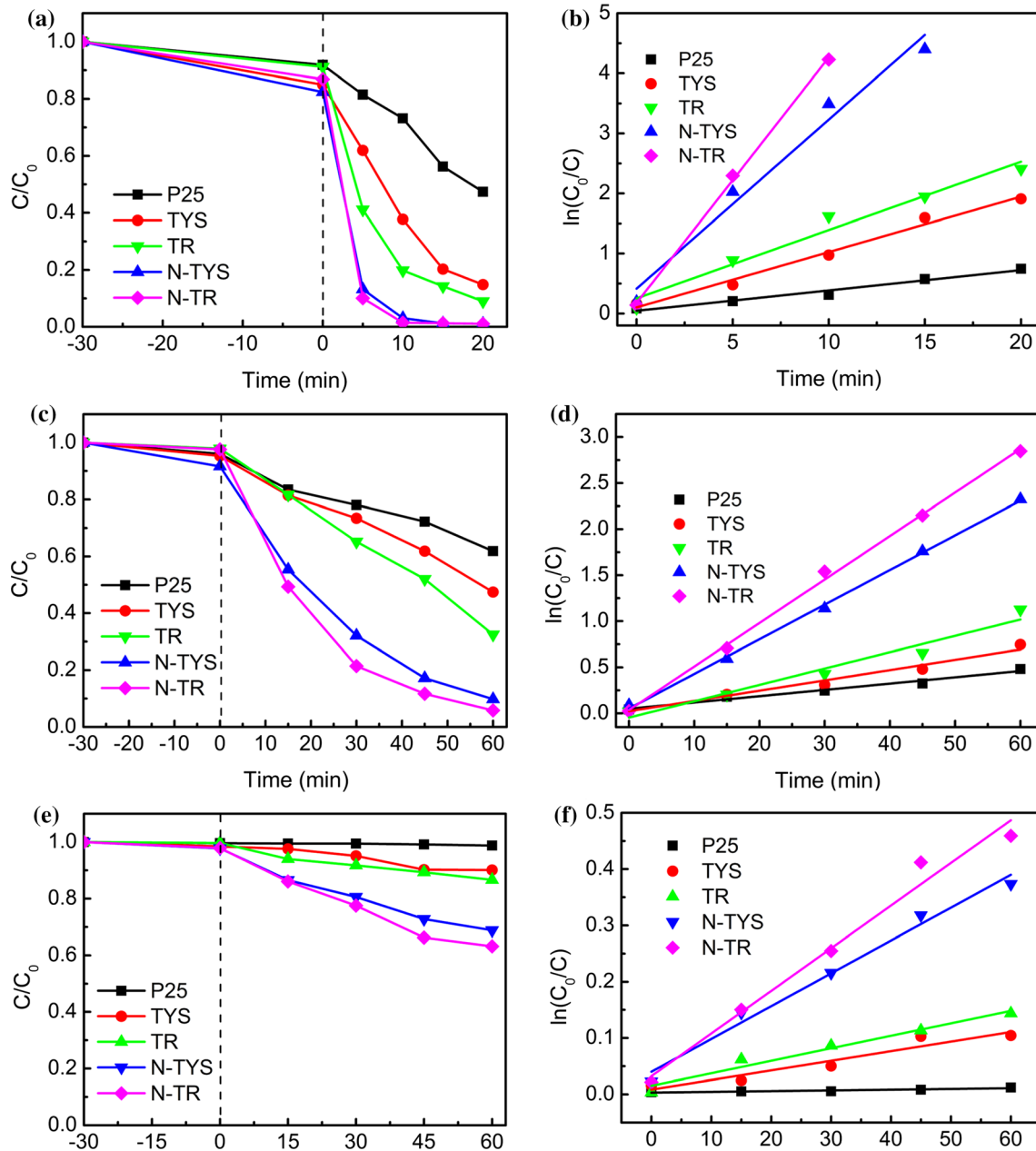


**Figure 9** Photocatalytic performance and kinetic linear simulation curves of TR, TYS, N-TR, N-TYS and P25 in the degradation of **a, b** RhB; **c, d** MB and **e, f** phenol under visible-light irradiation.

determined to be 0.0068, 0.0112, 0.0177, 0.0376 and 0.04723 min<sup>-1</sup>, and the photodegradation of phenol rate constant values is determined to be 0.0001, 0.0017, 0.0022, 0.0058 and 0.0076 min<sup>-1</sup>. Based on the above data, we can find that the degradation of RhB is the easiest, while phenol is relatively difficult. However, the performance law between the samples is unchanged, that is, the photodegradation rate: N-TR > N-TYS > TR > TYS > P25. To exclude the effect of dye self-degradation phenomenon, we also

carried out the blank experiments. Fig. S6 shows that RhB and phenol photodegradation are negligible without TiO<sub>2</sub> under visible-light illumination, while MB photodegradation is relatively serious.

In addition, the photodegradation performance of other samples with different intermediate amounts of precursor for the photodegradation of RhB was also investigated and is shown in Fig. S7. As precursor content increases from 0.43 to 6.88 g, the degradation rate decreases first and then rise. This result indicates

that in the photocatalytic field, the advantages of 1D and 3D hierarchical structures are obvious, and irregular transition morphology is not conducive to the improvement of photocatalytic performance (Fig. S7c).

Based on the above experimental results, several significant conclusions can be summarized. Firstly, it is clearly observed that photocatalytic activity of TR, TYS, N-TR, N-TYS is higher than that of P25, especially N-TR is 12 times than P25 for the photodegradation of RhB. It is generally accepted that P25 belongs to 0D nanoparticles with an average particle size of 25 nm. Interestingly, in our work, 1D micro-rods and 3D yolk-like spheres as hierarchical architectures are composed of 0D nanoparticles. The result confirms that unique superstructures have benefitted impact on photocatalytic capabilities. Moreover, the XRD pattern of N-TR hardly changes after degradation, indicating the stability of as-prepared samples (Fig. S8). Secondly, 1D rod-like structure exhibits higher photodegradation efficiency than 3D yolk-like structure, which ascribes to the reason that rod structure possesses unique properties such as relatively high specific area ( $190.8 \text{ m}^2 \text{ g}^{-1}$ , Table 1), relatively better crystallinity, direct electrical pathway and higher light utilization rate [24, 25]. Although the hierarchical yolk-like structure endows the N-TYS with sufficient interior space to capture photons, the narrow space of N-TR, which is formed among internal nanorods, makes it easier to increase multiple internal reflections of light [23]. In addition, 1D structure also benefits for charge separation and transport. Finally, the N-doped samples exhibit higher photodegradation efficiency than bare  $\text{TiO}_2$  because of the synergetic effects between enhanced visible-light harvesting capabilities and higher electron separation efficiency.

To further elucidate their intrinsic mechanism for photocatalytic degradation of RhB, the effect of active species of N-TR was investigated via radical trapping experiments. As shown in Fig. 10, after adding BQ and  $\text{Na}_2\text{-EDTA}$ , the degradation process of RhB is obviously suppressed, while IPA has a little effect on the degradation, indicating that the active species  $\cdot\text{O}_2^-$  and  $\text{h}^+$  play significant role in photocatalytic reaction but  $\cdot\text{OH}$ .

According to the above mentioned, we propose the mechanism for the visible-light photocatalytic reaction over N-doped  $\text{TiO}_2$  (Fig. 11). N doping can narrow the band gap and cause visible-light

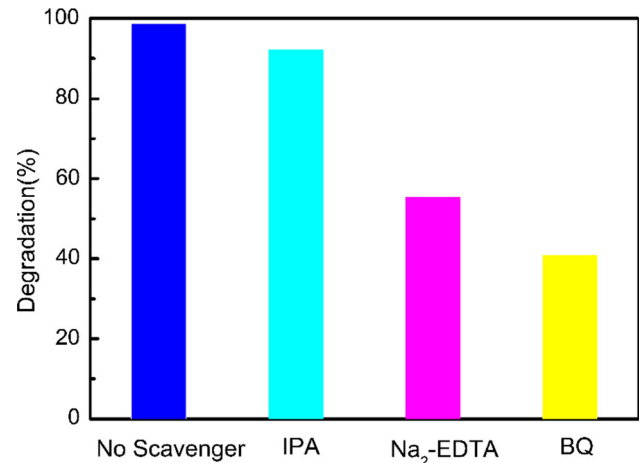


**Figure 10** Influence of various trapping agents on the RhB photodegradation in the presence of N-TR under visible-light irradiation.

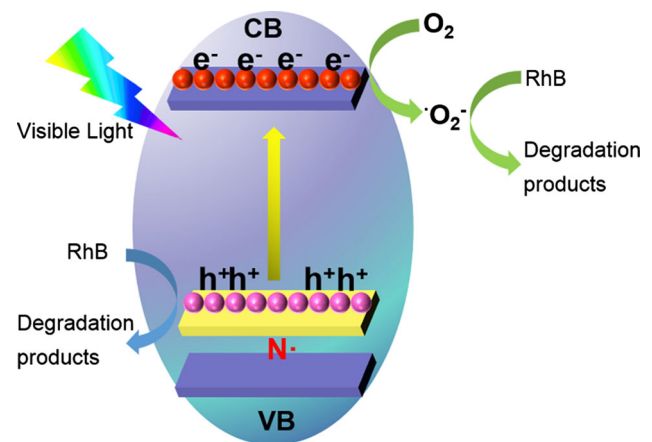


**Figure 11** Proposed photocatalytic mechanism for photodegradation of RhB under visible-light irradiation.

response, accounting for the visible-light absorption of N-doped samples. Under visible-light irradiation, N-TR and N-TYS can be excited and produce electrons and holes pairs. Subsequently, the electrons which transmitted to the conduction band react with  $\text{O}_2$  to produce active species  $\cdot\text{O}_2^-$ . The redox properties of  $\cdot\text{O}_2^-$  and  $\text{h}^+$  lead to rapid photocatalytic degradation of RhB.

## Conclusions

In summary, the tunable 1D rod-like and 3D yolk-like N-doped  $\text{TiO}_2$  hierarchical architectures were successfully fabricated by one-step solvothermal route via changing the precursor concentration. The



morphologies, one-dimension and three-dimension are caused by in situ growth and Ostwald ripening, respectively. The unique N-doped rod-like and yolk-like hierarchical structures significantly increase the specific surface area and light utilization rate; meanwhile, nitrogen doping expands the visible-light response range, both of which improve the photocatalytic performance compared with commercial P25. Furthermore, through the systematic comparison, N-doped 1D rod-like structure with the unique hierarchical structure and larger specific surface area exhibits the excellent performance in terms of photodegradation, charge separation ability and electron–hole recombination efficiency, indicating that the proper TiO<sub>2</sub> dimension with a large specific surface area is greatly promising technique for enhancement of photocatalysis. This work can provide a guidance for researchers in the field of morphology control.

## Acknowledgements

This work was supported by the National Natural Science Foundation of China (51772102, 51972114, 51902107); the National Natural Science Foundation of Guangdong Province (2019A1515011002, 2019A1515011992); the Guangdong YangFan Innovative & Entrepreneurial Research Team Program (2016YT03C327); Project funded by China Postdoctoral Science Foundation (2018M643074, 2019T120728); and Fundamental Research Funds for the Central Universities (2019MS002).

## Compliance with ethical standards

**Conflict of interest** No author has financial or other contractual agreements that might cause conflict of interest.

**Electronic supplementary material:** The online version of this article (<https://doi.org/10.1007/s10853-019-04247-4>) contains supplementary material, which is available to authorized users.

## References

- [1] Natarajan S, Bajaj HC, Tayade RJ (2018) Recent advances based on the synergistic effect of adsorption for removal of dyes from waste water using photocatalytic process. *J Environ Sci-China* 65:201–222
- [2] Nakata K, Ochiai T, Murakami T, Fujishima A (2012) Photoenergy conversion with TiO<sub>2</sub> photocatalysis: new materials and recent applications. *Electrochim Acta* 84:103–111
- [3] Liang HJ, Jia ZC, Zhang HC, Wang XB, Wang JJ (2017) Photocatalysis oxidation activity regulation of Ag/TiO<sub>2</sub> composites evaluated by the selective oxidation of Rhodamine B. *Appl Surf Sci* 422:1–10
- [4] Wang P, Jia CC, Li J, Yang P (2019) Ti<sup>3+</sup>-doped TiO<sub>2</sub>(B)/anatase spheres prepared using thioglycolic acid towards super photocatalysis performance. *J Alloy Compd* 780:660–670
- [5] Liu Q, Ding DY, Ning CQ, Wang XW (2015) Black Ni-doped TiO<sub>2</sub> photoanodes for high-efficiency photoelectrochemical water-splitting. *Int J Hydrogen Energy* 40:2107–2114
- [6] Darbandi M, Dickerson JH (2016) Nanoscale engineering of TiO<sub>2</sub> nanoparticles: evolution of the shape, phase, morphology, and facet orientation. *Mater Lett* 180:212–218
- [7] Sarkar B, Singhal N, Goyal R, Bordoloi A, Konathala LNS, Kumar U, Bal R (2016) Morphology-controlled synthesis of TiO<sub>2</sub> nanostructures for environmental application. *Catal Commun* 74:43–48
- [8] He XY, Zhang CL (2019) Recent advances in structure design for enhancing photocatalysis. *J Mater Sci* 54:8831–8851. <https://doi.org/10.1007/s10853-019-03417-8>
- [9] Zha RH, Nadimicherla R, Guo X (2015) Morphology engineering of nanostructured TiO<sub>2</sub> particles. *RSC Adv* 5:6481–6488
- [10] Verbruggen SW (2015) TiO<sub>2</sub> photocatalysis for the degradation of pollutants in gas phase: from morphological design to plasmonic enhancement. *J Photochem Photobiol C* 24:64–82
- [11] Dufour F, Pigeot-Remy S, Durupthy O et al (2015) Morphological control of TiO<sub>2</sub> anatase nanoparticles: What is the good surface property to obtain efficient photocatalysts? *Appl Catal B-Environ* 174:350–360
- [12] Sambandam B, Surenjan A, Philip L, Pradeep T (2015) Rapid synthesis of C-TiO<sub>2</sub>: tuning the shape from spherical to rice grain morphology for visible light photocatalytic application. *ACS Sustain Chem Eng* 3:1321–1329
- [13] Chen Y, Li WZ, Wang JY, Gan YL, Liu L, Ju MT (2016) Microwave-assisted ionic liquid synthesis of Ti<sup>3+</sup> self-doped TiO<sub>2</sub> hollow nanocrystals with enhanced visible-light photoactivity. *Appl Catal B-Environ* 191:94–105
- [14] Lv J, Gao HZ, Wang HG et al (2015) Controlled deposition and enhanced visible light photocatalytic performance of Pt-modified TiO<sub>2</sub> nanotube arrays. *Appl Surf Sci* 351:225–231

- [15] Yu X, Zhao ZH, Zhang J, Guo WB, Li LL, Liu H, Wang ZL (2017) One-step synthesis of ultrathin nanobelts-assembled urchin-like anatase TiO<sub>2</sub> nanostructures for highly efficient photocatalysis. *CrystEngComm* 19:129–136
- [16] Chen W, Wang Y, Liu S et al (2018) Non-noble metal Cu as a cocatalyst on TiO<sub>2</sub> nanorod for highly efficient photocatalytic hydrogen production. *Appl Surf Sci* 445:527–534
- [17] Wang H, Wu D, Wu W et al (2019) Preparation of TiO<sub>2</sub> microspheres with tunable pore and chamber size for fast gaseous diffusion in photoreduction of CO<sub>2</sub> under simulated sunlight. *J Colloid Interface Sci* 539:194–202
- [18] Anwer S, Bharath G, Iqbal S et al (2018) Synthesis of edge-site selectively deposited Au nanocrystals on TiO<sub>2</sub> nanosheets: an efficient heterogeneous catalyst with enhanced visible-light photoactivity. *Electrochim Acta* 283:1095–1104
- [19] Sharma PK, Cortes M, Hamilton JWJ, Han YS, Byrne JA, Nolan M (2019) Surface modification of TiO<sub>2</sub> with copper clusters for band gap narrowing. *Catal Today* 321:9–17
- [20] Colomer MT, del Campo A (2019) Preparation of nanostructured TiO<sub>2</sub> films with high catalytic activity and their 3D spatial distribution of anatase and rutile phases. *J Mater Sci* 54:9414–9425. <https://doi.org/10.1007/s10853-019-03550-4>
- [21] Devan RS, Patil RA, Lin JH, Ma YR (2012) One-dimensional metal-oxide nanostructures: recent developments in synthesis, characterization, and applications. *Adv Funct Mater* 22:3326–3370
- [22] Leng M, Chen Y, Xue JM (2014) Synthesis of TiO<sub>2</sub> nanosheets via an exfoliation route assisted by a surfactant. *Nanoscale* 6:8531–8534
- [23] Mohan Kumar K, Godavarthi S, Karthik TVK et al (2016) Green synthesis of S-doped rod shaped anatase TiO<sub>2</sub> microstructures. *Mater Lett* 183:211–214
- [24] Zhu K, Vinzant TB, Neale NR, Frank AJ (2007) Removing structural disorder from oriented TiO<sub>2</sub> nanotube arrays: reducing the dimensionality of transport and recombination in dye-sensitized solar cells. *Nano Lett* 7:3739–3746
- [25] Li SS, Chang CP, Lin CC et al (2011) Interplay of three-dimensional morphologies and photocarrier dynamics of polymer/TiO<sub>2</sub> bulk heterojunction solar cells. *J Am Chem Soc* 133:11614–11620
- [26] Zhang ZH, Wu HJ (2014) Multiple band light trapping in ultraviolet, visible and near infrared regions with TiO<sub>2</sub> based photonic materials. *Chem Commun* 50:14179–14182
- [27] Lei BX, Liao JY, Zhang R, Wang J, Su CY, Kuang DB (2010) Ordered crystalline TiO<sub>2</sub> nanotube arrays on transparent FTO glass for efficient dye-sensitized solar cells. *J Phys Chem C* 114:15228–15233
- [28] Gao M, Zhu L, Ong WL, Wang J, Ho GW (2015) Structural design of TiO<sub>2</sub>-based photocatalyst for H<sub>2</sub> production and degradation applications. *Catal Sci Technol* 5:4703–4726
- [29] Lou XW, Wang Y, Yuan C, Lee JY, Archer LA (2006) Template-free synthesis of SnO<sub>2</sub> hollow nanostructures with high lithium storage capacity. *Adv Mater* 18:2325–2329
- [30] Chen G, Cheng H, Zhang W, Yang Z, Qiu M, Zhu X, Chen M (2015) Template-free synthesis of single-/double-walled TiO<sub>2</sub> nanovesicles: potential photocatalysts for engineering application. *AIChE J* 61:1478–1482
- [31] Yang J, Wen ZH, Shen XX, Dai J, Li Y, Li YJ (2018) A comparative study on the photocatalytic behavior of graphene-TiO<sub>2</sub> nanostructures: effect of TiO<sub>2</sub> dimensionality on interfacial charge transfer. *Chem Eng J* 334:907–921
- [32] Aoi Y, Kobayashi S, Kamijo E, Deki S (2005) Fabrication of three-dimensional ordered macroporous titanium oxide by the liquid-phase deposition method using colloidal template. *J Mater Sci* 40:5561–5563. <https://doi.org/10.2472/jms.53.1313>
- [33] Paramasivam I, Jha H, Liu N, Schmuki P (2012) A review of photocatalysis using self-organized TiO<sub>2</sub> nanotubes and other ordered oxide nanostructures. *Small* 8:3073–3103
- [34] Dong F, Zhao WR, Wu ZB (2008) Characterization and photocatalytic activities of C, N and S co-doped TiO<sub>2</sub> with 1D nanostructure prepared by the nano-confinement effect. *Nanotechnology* 19:365607–365616
- [35] Chen K, Fan QH, Chen CL, Chen ZS, Alsaedi A, Hayat T (2019) Insights into the crystal size and morphology of photocatalysts. *J Colloid Interface Sci* 538:638–647
- [36] Li HX, Bian ZF, Zhu J et al (2007) Mesoporous titania spheres with tunable chamber structure and enhanced photocatalytic activity. *J Am Chem Soc* 129:8406–8407
- [37] Zeng L, Song WL, Xie CS (2014) Fabrication of TiO<sub>2</sub> rod in tube nanostructure with enhanced photocatalytic activity: investigation of the effect of the states of the precursor on morphology. *RSC Adv* 4:36708–36712
- [38] Yang XY, Peng HL, Zou ZM et al (2018) Diethylenediamine-assisted template-free synthesis of a hierarchical TiO<sub>2</sub> sphere-in-sphere with enhanced photocatalytic performance. *Dalton T* 47:16502–16508
- [39] Ye T, Chen W, Xu H, Geng NN, Cai Y (2018) Preparation of TiO<sub>2</sub>/graphene composite with appropriate N-doping ratio for humic acid removal. *J Mater Sci* 53:613–625. <https://doi.org/10.1007/s10853-017-1509-4>
- [40] Yang GD, Jiang Z, Shi HH, Xiao TC, Yan ZF (2010) Preparation of highly visible-light active N-doped TiO<sub>2</sub> photocatalyst. *J Mater Chem* 20:5301–5309
- [41] Li X, Liu P, Mao Y, Xing M, Zhang J (2015) Preparation of homogeneous nitrogen-doped mesoporous TiO<sub>2</sub> spheres with enhanced visible-light photocatalysis. *Appl Catal B-Environ* 164:352–359

- [42] Kruk M, Jaroniec M (2001) Gas adsorption characterization of ordered organic-inorganic nanocomposite materials. *Chem Mater* 13:3169–3183
- [43] Liu C, Zhang L, Liu R et al (2016) Hydrothermal synthesis of N-doped TiO<sub>2</sub> nanowires and N-doped graphene heterostructures with enhanced photocatalytic properties. *J Alloy Compd* 656:24–32
- [44] Lin Z, Waller G, Liu Y, Liu M, Wong C-P (2012) Facile synthesis of nitrogen-doped graphene via pyrolysis of graphene oxide and urea, and its electrocatalytic activity toward the oxygen-reduction reaction. *Adv Energy Mater* 2:884–888
- [45] Chen CS, Liu XY, Long H, Ding F, Liu QC, Chen XA (2019) Preparation and photocatalytic performance of graphene Oxide/WO<sub>3</sub> quantum Dots/TiO<sub>2</sub>@SiO<sub>2</sub> microspheres. *Vacuum* 164:66–71
- [46] Tian G, Chen Y, Bao H-L et al (2012) Controlled synthesis of thorny anatase TiO<sub>2</sub> tubes for construction of Ag-AgBr/TiO<sub>2</sub> composites as highly efficient simulated solar-light photocatalyst. *J Mater Chem* 22:2081–2088
- [47] Tian GH, Chen YJ, Zhou W, Pan K, Tian CG, Huang XR, Fu HG (2011) 3D hierarchical flower-like TiO<sub>2</sub> nanostructure: morphology control and its photocatalytic property. *CrytEngComm* 13:2994–3000
- [48] Zhang Y, Wang CW, Hou HS, Zou GQ, Ji XB (2017) Nitrogen doped/carbon tuning yolk-like TiO<sub>2</sub> and its remarkable impact on sodium storage performances. *Adv Energy Mater* 7:1600173–1600184
- [49] Bao Y, Kang QL, Ma JZ, Liu C (2017) Monodisperse hollow TiO<sub>2</sub> spheres for thermal insulation materials: template-free synthesis, characterization and properties. *Ceram Int* 43:8596–8602
- [50] Hua Chun Z (2007) Ostwald ripening: a synthetic approach for hollow nanomaterials. *Curr Nanosci* 3:177–181
- [51] Nguyen DT, Kim K-S (2016) Self-development of hollow TiO<sub>2</sub> nanoparticles by chemical conversion coupled with Ostwald ripening. *Chem Eng J* 286:266–271
- [52] Yang HG, Zeng HC (2004) Preparation of hollow anatase TiO<sub>2</sub> nanospheres via Ostwald ripening. *J Phys Chem B* 108:3492–3495
- [53] Di Valentin C, Finazzi E, Pacchioni G, Selloni A, Livraghi S, Paganini MC, Giamello E (2007) N-doped TiO<sub>2</sub>: theory and experiment. *Chem Phys* 339:44–56
- [54] Prakash K, Karuthapandian S, Senthilkumar S (2019) Zeolite nanorods decorated g-C<sub>3</sub>N<sub>4</sub> nanosheets: a novel platform for the photodegradation of hazardous water contaminants. *Mater Chem Phys* 221:34–56
- [55] Chen CS, Cao SY, Long H et al (2015) Highly efficient photocatalytic performance of graphene oxide/TiO<sub>2</sub>-Bi<sub>2</sub>O<sub>3</sub> hybrid coating for organic dyes and NO gas. *J Mater Sci-Mater Electron* 26:3385–3391

**Publisher's Note** Springer Nature remains neutral with regard to jurisdictional claims in published maps and institutional affiliations.